Journal of Molecular Structure 1035 (2013) 101–108

Contents lists available at SciVerse ScienceDirect

Journal of Molecular Structure

journal homepage: www.elsevier.com/locate/molstruc

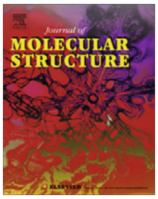

Defect structures and optical characteristics of Er^{3+} ion in $Er:LiNbO_3$ crystals

Yannan Qian [a], Rui Wang [b,*], Biao Wang [a,*], Chao Xu [b], Lili Xing [b], Yanling Xu [b]

[a] *School of Physics and Engineering, Sun Yat-sen University, Guangzhou 510275, China*
[b] *Department of Chemistry, Harbin Institute of Technology, Harbin 150001, China*

HIGHLIGHTS

- ▶ OH^- and UV–vis-near infrared absorption spectra of $Er:LiNbO_3$ crystals.
- ▶ Stokes and anti-stokes luminescence spectra of $Er:LiNbO_3$ and $Zn/Er:LiNbO_3$.
- ▶ Relation between structural and optical characteristics of $Er:LiNbO_3$ crystals.
- ▶ Near infrared emission spectra of $Er:LiNbO_3$ crystals under 980 nm excitation.
- ▶ J–O parameters, absorption and emission cross section spectra are discussed.

ARTICLE INFO

Article history:
Received 15 August 2012
Received in revised form 14 September 2012
Accepted 14 September 2012
Available online 25 September 2012

Keywords:
$Er:LiNbO_3$
Defect structure
Stokes and anti-stokes luminescence spectra
Near infrared emission spectra
Judd–Ofelt, Füchtbauer–Ladenburg and McCumber theory

ABSTRACT

Congruent $Er:LiNbO_3$ crystals were grown by Czochraski method. The OH^- absorption and UV–vis-near infrared absorption spectra indicated that Er^{3+} cluster sites were formed in $LiNbO_3$ crystal doped with 3 mol% Er^{3+} ions. Studies on the stokes and anti-stokes spectra showed that the formation of Er^{3+} cluster sites could increase the rate of cross relaxation processes. Judd–Ofelt theory was carried out to discuss the spectral characteristics of Er^{3+} ions in $Er:LiNbO_3$ crystals. Based on Füchtbauer–Ladenburg and McCumber theory, the emission cross section of the $^4I_{13/2} \rightarrow {}^4I_{15/2}$ transition of Er^{3+} ion was calculated, and the potential laser performance was evaluated by the gain cross section spectra. $Er:LiNbO_3$ crystal codoped with Zn^{2+} ions was also grown to discuss the relation between the defect structure and optical characteristics of Er^{3+} ion.

1. Introduction

$Er:LiNbO_3$ crystal has attracted tremendous research interest since it combines the nonlinear optical properties of $LiNbO_3$ with the amplifying and lasing characteristics of Er^{3+} ion [1–3]. The upconversion (UC) emission arising from the activated rare-earth ions is important for practical applications such as UC laser, biological imaging, temperature sensors, biolabels and DNA detection [4–6]. In particular, owing to electronic energy level scheme of Er^{3+} ion allowing for many radiative transitions, it becomes an ideal candidate for upconversion emission [7,8]. The near infrared emission around wavelength of 1.54 μm arising from the $^4I_{13/2} \rightarrow {}^4I_{15/2}$ transition of Er^{3+} ion is eye-safe and matches well the third telecommunication window [9,10]. At present, $Er:LiNbO_3$ crystal has been successfully applied in the Erbium-doped fiber amplifier (EDFA) which is one of the key elements employed in the wavelength-division-multiplexing (WDM) network of optical communication [11,12].

To meet the practical application requirements of fluorescence, many researches on manipulating UC color output of rare-earth ion have been developed. It has been reported that adjusting the rate of cross relaxation processes, such as $^5S_2/^5F_4$ (Ho) + $^2F_{5/2}$ (Ce) → $^5F_5$ (Ho) + $^2F_{7/2}$ (Ce) and $^5I_6$ (Ho) + $^2F_{5/2}$ (Ce) → $^5I_7$ (Ho) + $^2F_{7/2}$ (Ce), could tune the UC emission from green to red in $Yb^{3+}/Ho^{3+}:NaYF_4$ nanocrystals tridoped with Ce^{3+} ions [13]. F. Vetrone has reported that the increased rate of cross relaxation process ($^4F_{7/2} + {}^4I_{11/2} \rightarrow {}^4F_{9/2} + {}^4F_{9/2}$) leads to an enhancement of red UC emission and a reduction of green emission in $Er^{3+}:Y_2O_3$ samples under 980 nm excitation [14]. Studies on these previous works indicated the optical characteristics of rare-earth ion may be governed by the rate of cross relaxation mechanisms. As for $Er:LiNbO_3$ crystal, the defect structure in crystal lattice affected the

---

* Corresponding authors.
E-mail addresses: wangrui001@hit.edu.cn (R. Wang), wangbiao@mail.sysu.edu.cn (B. Wang).

0022-2860/$ - see front matter © 2012 Elsevier B.V. All rights reserved.
http://dx.doi.org/10.1016/j.molstruc.2012.09.039

fluorescence efficiency [15]. A decreased green UC emission and the enhancement of near infrared emission were observed via adjusting the distribution of Er^{3+} ion in $Er:LiNbO_3$ crystal. However, despite the extensive investigations on $Er:LiNbO_3$ crystals for optical characteristics of Er^{3+} ions were reported, few reports on the relation between the defect structure of $LiNbO_3$ crystal and the optical characteristics of Er^{3+} ion have appeared in the literature.

In this paper, $LiNbO_3$ doped with 0.5, 1 and 3 mol% Er^{3+} ions and $Er:LiNbO_3$ codoped with Zn^{2+} ions were grown by Czochralski technique. The concentration of Er^{3+} ions in the crystal was determined by the inductively coupled plasma mass spectrometry (ICP-MS). The OH^- absorption and UV–vis-near infrared absorption spectra of $Er:LiNbO_3$ crystals were measured to study the defect structure of crystal lattice. The stokes and anti-stokes luminescence emission spectra were used to investigate the relation between the dopant occupancy and optical characteristic of Er^{3+} ion in $Er:LiNbO_3$ crystals. The Judd–Ofelt intensity parameters of $Er:LiNbO_3$ crystals were calculated, and the absorption and emission cross section spectra, as well as the gain cross section spectra of ${}^4I_{13/2} \rightarrow {}^4I_{15/2}$ transition in Er-3 crystal as a function of P ranging from 0 to 1 were studied.

2. Experimental

Congruent $LiNbO_3$ crystals doped with 0.5, 1 and 3 mol% Er^{3+} ions were grown along the ferroelectric c axis by Czochralski technique. Er^{3+} (3 mol%):$LiNbO_3$ crystal codoped with 6 mol% Zn^{2+} ions was also grown. An axial temperature gradient of 40–50 K/cm, the rotating rate of 10–25 rpm and the pulling rate of 0.5–2 mm/h were chosen to grow these crystals. The grown crystals were polarized at 1200 °C with a current density of 5 mA/cm^2. The boules were cut into Y-cut plates ($X \times Y \times Z = 10 \times 2 \times 10\ mm^3$) with carefully polished surfaces. The three crystals are named as Er-0.5, Er-1 and Er-3, respectively.

The Er content ($[Er^{3+}]/[Nb^{5+}]$ ratio) in the crystal was determined by the inductively coupled plasma mass spectrometry (ICP-MS, Optima 7500 Series, Agilent Technologies Inc., Beijing). The OH^- absorption spectra were measured by Fourier-Transform spectrophotometer (Niconet-710, Nicolet, USA). The CARY spectrophotometer was used to measure the ultraviolet–visible (UV–vis)-infrared absorption spectra in the range from 300 to 1650 nm. A power-controllable 980 nm diode laser was used to measure the upconversion and near infrared emission spectra. All fluorescence emissions were recorded at the same geometry by using the spectrometer (Bruker optics 500IS/SM) equipped with a semiconductor cooled charge coupled device detector (DV440, Andor).

3. Results and discussion

The estimated Er contents ($[Er^{3+}]/[Nb^{5+}]$ ratio) in the crystal are given in Table 1. It is well known that the segregation coefficient is defined as the ratio of the ion concentration in the crystal to that in the melt. As illustrated in Table 1, the segregation coefficient of Er^{3+} ion decreases with the increasing concentration of Er^{3+} ions in the melt.

Table 1
Molar compositions of Er^{3+} ion in melt/crystal and the concentration of Er^{3+} ions.

	Er-0.5	Er-1	Er-3
$[Er^{3+}]/[Nb^{5+}]$ content in melt/(mol%)	0.5	1	3
The segregation coefficient of Er^{3+} ion	1.54	1.51	1.47
$[Er^{3+}]/[Nb^{5+}]$ content in crystal/(mol%)	0.77	1.51	4.41
Er^{3+} concentration in crystal ($\times 10^{20}\ cm^{-3}$)	1.454	2.85	8.33

3.1. OH^- absorption spectra

The OH^- absorption spectra of Er-0.5, Er-1 and Er-3 crystals, shown in Fig. 1, illustrate that the OH^- peaks of the three crystals are at 3486 cm^{-1}, 3489 cm^{-1} and 3495 cm^{-1}, respectively. are at 3486 cm^{-1}, 3489 cm^{-1} and 3495 cm^{-1}, respectively. Li vacancy defect model has been established as one of the most popular model for understanding the defect structure of $LiNbO_3$ crystal doped with rare-earth ions [16]. As for congruent ($[Li]/[Nb] = 0.946$) $LiNbO_3$ crystal, the lithium-deficient leads to the formation of intrinsic defect antisites Nb_{Li}^{4+} (the Nb^{5+} ions locate in Li sites). As well known, the stretching vibration of $Nb_{Li}^{4+}{-}OH^-$ in pure $LiNbO_3$ crystal appears at 3483 cm^{-1} in the OH^- absorption spectra. When Er^{3+} ion enters into $LiNbO_3$ crystal lattice, it replaces the antisite Nb_{Li}^{4+} firstly, and the Er_{Li}^{2+} defect is formed. The 3486 cm^{-1} OH^- peak in Er-0.5 is attributed to the overlapping stretching vibration of $Nb_{Li}^{4+}{-}OH^-$ and $Er_{Li}^{2+}{-}OH^-$ [17]. In the case of Er-1 and Er-3 crystals, 3489 cm^{-1} and 3495 cm^{-1} OH^- peaks correspond to the stretching vibration of $Er_{Li}^{2+}{-}OH^-$ and $Er_{Li}^{2+}{-}OH^-{-}Er_{Nb}^{2-}$, respectively [18]. The presence of $Er_{Li}^{2+}{-}OH^-{-}Er_{Nb}^{2-}$ means the formation of Er^{3+} cluster sites in Er-3 crystal, which consist of one Er_{Li} site and one Er_{Nb} site.

3.2. UV–vis-near infrared absorption spectra

Fig. 2 shows UV–vis-near infrared absorption spectra of Er-0.5, Er-1 and Er-3 crystals. The absorption bands centered at 368, 381, 410, 453, 492, 525, 550, 660, 980 and 1540 nm are attributed to the transitions from the ground ${}^4I_{15/2}$ state to the ${}^4G_{9/2}$, ${}^4G_{11/2}$, ${}^2H_{9/2}$, ${}^4F_{3/2}$, ${}^4F_{7/2}$, ${}^2H_{11/2}$, ${}^4S_{3/2}$, ${}^4F_{9/2}$, ${}^4I_{11/2}$ and ${}^4I_{13/2}$ states of Er^{3+} ion. The inset is the partial enlarged UV absorption spectra in the range from 310 nm to 340 nm. It can be seen from the inset that the absorption edge positions of Er-0.5, Er-1 and Er-3 crystals are 321 nm, 330 nm and 322 nm, respectively. Generally, the redshift of absorption edge is ascribed to the decreasing valence electron transition energy which is caused by the higher polarization ability of the doped ion than that of the replaced ion. As for $Er:LiNbO_3$ crystal, the calculated polarization abilities of Nb^{5+}, Er^{3+} and Li^+ are 52.5, 45.9 and 4.2, respectively [19]. Therefore, the fact that Li^+ ion is replaced by Er^{3+} ion with the large polarization ability causes the redshift of absorption edge. In contrast, the blueshift is attributed to the large polarization ability of Nb^{5+} ion substituted by Er^{3+} ion. Compared with the absorption edge at 322 nm of pure $LiNbO_3$ crystal, 0.5 mol% Er^{3+} ions doping leads to little blueshift. This is because Er^{3+} ion substitutes the larger polarization ability of intrinsic defect antisites Nb_{Li}^{4+} (Nb^{5+} ion locates Li site). The redshift of absorption edge from Er-0.5 (321 nm) to Er-1 (330 nm)

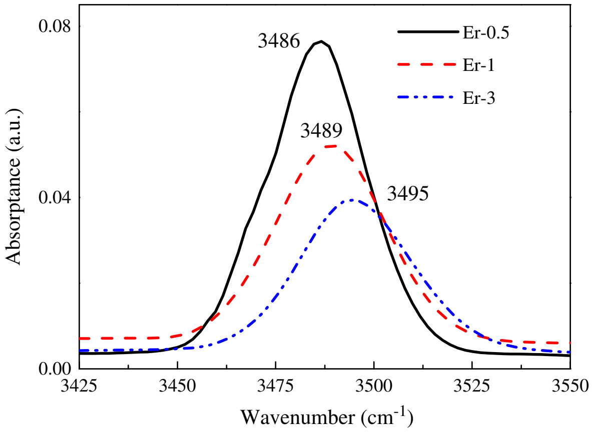

Fig. 1. The OH^- absorption spectra of $Er:LiNbO_3$ crystals.

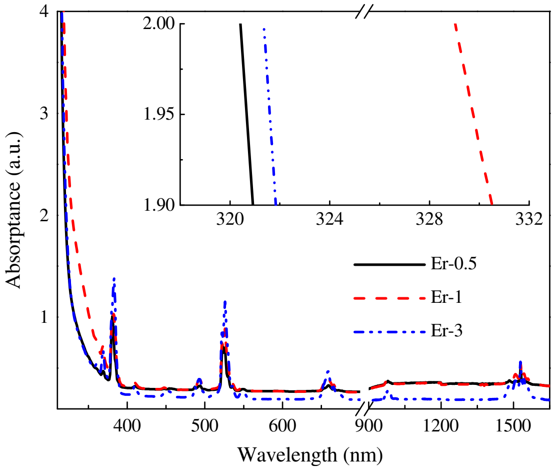

Fig. 2. UV–visible-near infrared absorption spectra of Er:LiNbO$_3$ crystals. The inset is the partial enlarged UV absorption spectra.

implies that Er^{3+} ion replaces Li^{+} ion, and Er_{Li}^{2+}—OH^{-} defects are formed. The blueshift in Er-3 relative to Er-1 crystal indicates that Er^{3+} ion begins to occupy the natural Nb^{5+} ion. Consequently, there are Er^{3+} cluster sites (Er_{Li}^{2+}—OH—Er_{Nb}^{2-}) in Er-3 crystal, in agreement with the experimental results shown in OH^{-} absorption spectra.

According to the absorption cross section, namely, the optical transition strength, the defect structure in Er:LiNbO$_3$ crystals could be studied further. The absorption cross section can be calculated by the following formula [20]:

$$\sum_{band} = \int_{band} \sigma(\lambda) d\lambda = \sum_{band} \frac{\alpha(\lambda)}{C} d\lambda \tag{1}$$

where $\sigma(\lambda)$ is the absorption cross section at the wavelength of λ, which is defined by α/C, α is the absorption coefficient and can be obtained from Fig. 2. C is the concentration of Er^{3+} ion in the crystal (see Table 1). Table 2 shows the calculated absorption cross sections of Er-0.5, Er-1 and Er-3 crystals.

As illustrated in Table 2, the absorption cross section of $^4G_{9/2}$/$^2H_{9/2}$/$^4F_{3/2}$/$^4F_{7/2}$/$^4S_{3/2}$/$^4F_{9/2}$ → $^4I_{15/2}$ transitions in Er-1 is larger than that in Er-0.5. However, all absorption cross section of transitions, except for that of $^4G_{9/2}$ → $^4I_{15/2}$ transition, decrease drastically when the concentration of Er^{3+} ions increases to 3 mol%. Gill has reported that the absorption cross section of Er^{3+} cluster site is smaller than that of the Er^{3+} isolated site [21]. Therefore, the reduction of absorption cross section caused by doping 3 mol% Er^{3+} ions suggests that the Er^{3+} cluster sites (Er_{Li}^{2+}—Er_{Nb}^{2-}) are formed in Er-3 crystal.

3.3. Defect structure of Er:LiNbO$_3$ crystal

In order to understand the effect of Er^{3+} occupancy in crystal lattice on the optical characteristics of Er^{3+} ion, the sketch map of LiNbO$_3$ and Er:LiNbO$_3$ crystals is given in Fig. 3. Er_{Li}^{2+} and Er_{Nb}^{2-} represent that Er^{3+} ions occupy Li and Nb sites, respectively. It is obvious that the distance between Er_{Li}^{2+}—Er_{Nb}^{2-} is shorter than that of Er_{Li}^{2+}-Er_{Li}^{2+} or Er_{Nb}^{2-}—Er_{Nb}^{2-}. It is well known that the efficiency of luminescence is dependent on the pump power, the concentration of rare-earth ion, the rate of cross relaxation process. The rate of cross relaxation (CR) process is inversely proportional to the distance between two neighboring ions. The CR process can readily occur when the distance between ions is small enough. Consequently, the formation of the Er^{3+} cluster sites (Er_{Li}^{2+}—Er_{Nb}^{2-}) will decrease the cross relaxation probabilities. The detailed discusses on the relation between the occupancy and the optical characteristics of Er^{3+} ion will be explained in a subsequent section.

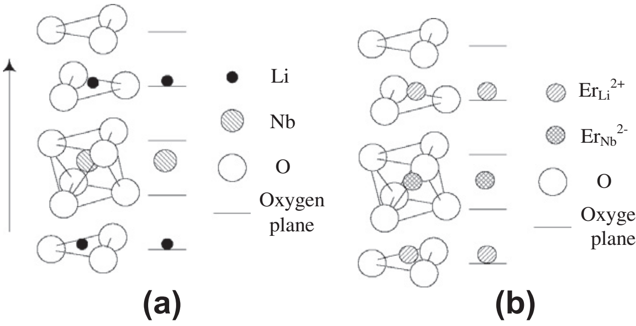

Fig. 3. Sketch map of LiNbO$_3$ and Er:LiNbO$_3$ crystals.

3.4. Stokes luminescence spectra

The stokes luminescence spectra of LiNbO$_3$ crystal doped with various concentrations of Er^{3+} ions (0.5, 1 and 3 mol%) under 476 nm diode laser are shown in Fig. 4, which exhibit a strong green emission centered at 550 nm and a weak red emission at 660 nm (enlarged five times). The green and red emissions are assigned to the transitions from the $^4S_{3/2}$ and $^4F_{9/2}$ states to the $^4I_{15/2}$ ground state, respectively. It is obvious that the green emission increases with Er^{3+} ions of 1 mol%, and decreases at 3 mol%. The red emission almost remains constant at 1 and 3 mol% Er^{3+} concentrations. The energy levels of Er^{3+} ion as well as the possible cross relaxation processes under 476 nm excitation are shown in Fig. 5. By directly exciting to the $^4F_{7/2}$ state, Er^{3+} ions at this state relax nonradiatively to the green emitting $^4S_{3/2}$ state and further to the red emitting $^4F_{9/2}$ state. Due to the large population of the $^4F_{7/2}$ state, three CR processes may occur: CR1: $^4S_{3/2} + {}^4I_{15/2} \rightarrow {}^4I_{9/2} + {}^4I_{13/2}$, CR2: $^4F_{7/2} + {}^4I_{15/2} \rightarrow {}^4I_{11/2} + {}^4I_{11/2}$ and CR3: $^2H_{11/2} + {}^4I_{11/2} \rightarrow {}^4F_{9/2} + {}^4F_{9/2}$. It is obvious that these CR processes will depopulate the $^4S_{3/2}$ state and then reduce the intensity of green emission. Therefore, the reduction of the green emission means the increased probability of CR processes in Er-3 crystal. Since CR probability is inversely proportional to the distance between two neighboring ions, the increased CR probability implies the formation of Er^{3+} cluster sites (Er_{Li}^{2+}—Er_{Nb}^{2-}) which have the short distance between the two neighboring Er^{3+} ions. Consequently, the experimental results suggest that the Er^{3+} cluster sites indeed enhance the probability of CR processes in Er:LiNbO$_3$ crystal.

Table 2
Absorption cross sections of Er:LiNbO$_3$ in the UV–visible-near infrared region.

Sample	Absorption cross sections ($\times10^{-21}$ cm^2)									
	$^4G_{9/2}$	$^4G_{11/2}$	$^2H_{9/2}$	$^4F_{3/2}$	$^4F_{7/2}$	$^2H_{11/2}$	$^4S_{3/2}$	$^4F_{9/2}$	$^4I_{11/2}$	$^4I_{13/2}$
Er-0.5	1.03	25.87	0.89	0.93	3.30	26.6	0.82	6.79	5.79	44.0
Er-1	1.08	16.14	1.10	1.25	3.66	20.0	0.87	8.57	4.72	39.5
Er-3	1.41	9.44	0.73	0.88	2.36	11.5	0.52	5.33	3.01	22.2

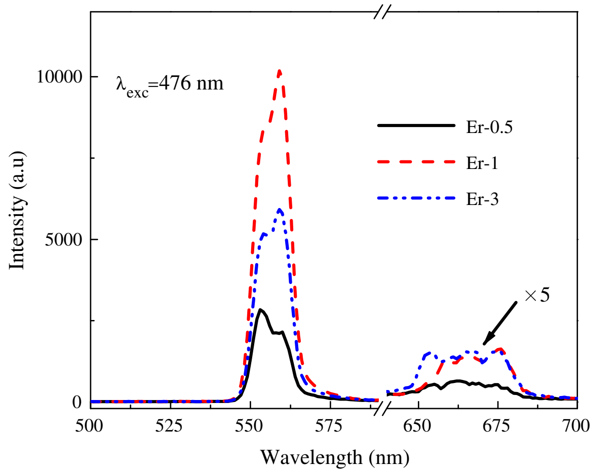

Fig. 4. The stokes luminescence spectra of Er:LiNbO$_3$ crystals under 476 nm excitation.

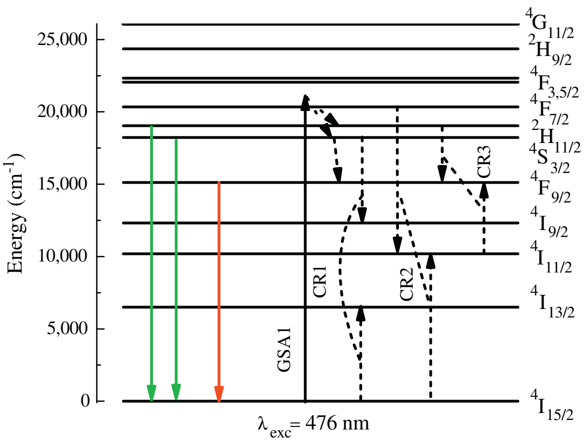

Fig. 5. The energy level of Er^{3+} ion as well as the possible cross relaxation processes under 476 nm excitation.

3.5. Anti-stokes luminescence spectra

The anti-stokes luminescence spectra of Er-0.5, Er-1 and Er-3 crystals under 800 nm and 980 nm excitation are illustrated in Fig. 6a and b, respectively. The green UC emissions centered at 525/550 nm are attributed to the $^2H_{11/2}/^4S_{3/2} \rightarrow {}^4I_{15/2}$ transition of Er^{3+} ion. The red UC emission arises from the $^4F_{9/2} \rightarrow {}^4I_{15/2}$ transition [22]. As shown in Fig. 6a, the green UC emission increases slightly with the increasing concentration of Er^{3+} ions, and a dramatically enhancement of red emission is observed for Er-3 crystal. Under 980 nm excitation (shown in Fig. 6b), both intensities of green and red UC emissions increase with the enhanced concentration of Er^{3+} ions.

In order to understand the upconversion mechanism, log–log plots of the fluorescent intensity (I_f) as a function of pump power (P) are measured and shown in Fig. 7. The required number of photons (n) to populate the green emitting state can be obtained by the relation $I_f \propto P^n$ for an unsaturated UC process [23]. As illustrated in Fig. 7a, the green UC emissions at 525/550 nm yield $n = 1.96$, 1.94 and 1.64, respectively, for Er-0.5, Er-1 and Er-3 crystals under 800 nm excitation. This is an indication that two 800 nm photons are needed to populate the green emitting states. Under 980 nm excitation (Fig. 7b), the slope n values are observed to be 2.74 and 2.68 for Er-0.5 and Er-1, respectively. The slope n values, which are larger than 2, indicate the participation of a three-photon process in addition to the two-photon process to populate the green upconversion emission. In the case of Er-3 crystal, the slope n values are 2.30 and 0.95 at the low and high pump power, respectively, which were discussed in Ref. [24].

Fig. 8a and b illustrates the UC mechanism as well as the proposed CR processes under the 800 nm and 980 nm excitation, respectively. Under 800 nm excitation (Fig. 8a), the green emitting $^2H_{11/2}/^4S_{3/2}$ states are populated via two pathways: The first one is the nonradiative relaxation from the $^2H_{9/2}$ state which is populated through GSA2: $^4I_{15/2}$ + a 800 nm photon → $^4I_{9/2}$ and ESA1: $^4I_{9/2}$ + a 800 nm photon → $^2H_{9/2}$. The other one is fed from ESA2: $^4I_{13/2}$ + a 800 nm photon → $^2H_{11/2}$. The two CR processes (CR4: $^2H_{11/2} + {}^4I_{13/2} \rightarrow {}^4I_{11/2} + {}^4F_{9/2}$ and CR5: $^4F_{7/2} + {}^4I_{11/2} \rightarrow {}^4F_{9/2} + {}^4F_{9/2}$) are contribution to the population of red emitting $^4F_{9/2}$ state. It is obvious that the increased probability of CR4 and CR5 processes would lead to a decreasing population of the $^4S_{3/2}/^2H_{11/2}$ states and in turn a higher population in the $^4F_{9/2}$ state which increases the red UC emission. From the view point of the defect structure of Er:LiNbO$_3$ crystal, the presence of Er^{3+} cluster sites in Er-3 crystal enhances the probability of CR processes, and then results in an increased

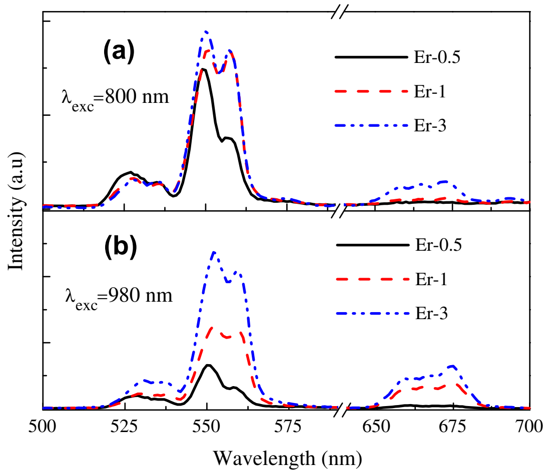

Fig. 6. The anti-stokes luminescence spectra of Er-0.5, Er-1 and Er-3 crystals: (a) under 800 nm excitation and (b) under 980 nm excitation.

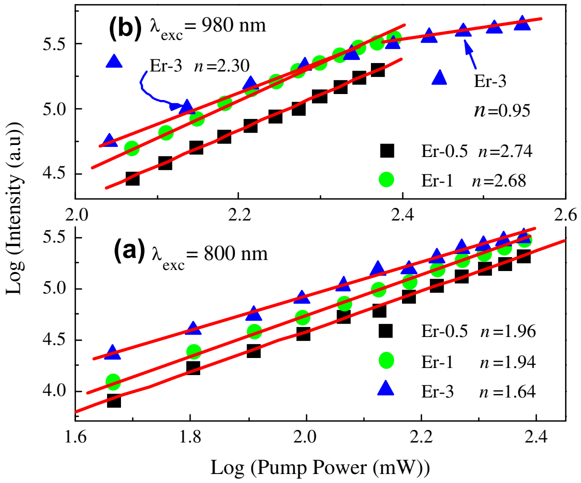

Fig. 7. Log–log plots of the intensity (I_f) of green UC emission as a function of pump power (P).

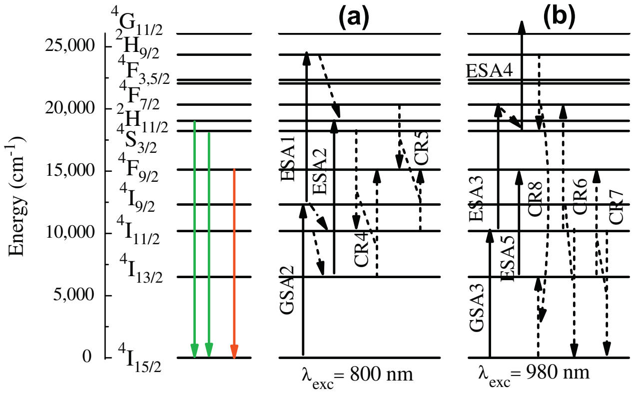

Fig. 8. The UC mechanism as well as the proposed CR processes: (a) under 800 nm excitation and (b) under 980 nm excitation.

intensity of red UC emission, in agreement with the experimental results shown in Fig. 6a.

As illustrated in Fig. 8b, the two- and three-photon process to populate the green emitting $^2H_{11/2}/^4S_{3/2}$ states were indicated in detail in Refs. [25,26], which thereby is only briefly described as follows: As for the two-photon process, the $^4F_{7/2}$ state is populated by GSA3: $^4I_{15/2}$ + a 980 nm photon → $^4I_{11/2}$ and ESA3: $^4I_{11/2}$ + a 980 nm photon → $^4F_{7/2}$. Subsequently, the Er^{3+} ions at the $^4F_{7/2}$ state nonradiatively relax $^2H_{11/2}/^4S_{3/2}$ state. The three-photon process of green emitting state is populated through nonradiatively relaxation from the $^4G_{11/2}$ state which is populated via GSA3, ESA3 and ESA4 ($^4S_{3/2}$ + a photon → $^4G_{11/2}$).

The possible CR processes can be expressed as follows:

CR6: $^4I_{11/2} + {}^4I_{11/2} \rightarrow {}^4F_{7/2} + {}^4I_{15/2}$;
CR7: $^4I_{13/2} + {}^4I_{11/2} \rightarrow {}^4F_{9/2} + {}^4I_{15/2}$;
CR8: $^2H_{9/2} + {}^4I_{11/2} \rightarrow {}^4F_{7/2} + {}^4I_{15/2}$.

It can be seen from Fig. 6b that the intensities of the green and red UC emissions are mainly dependent on the concentration of Er^{3+} ions under 980 nm excitation. For the constant Er^{3+} ions, it is believed that the relation between the defect structure and the optical characteristics of Er^{3+} ion under 980 nm excitation also complies that under 476 and 800 nm excitation. That is the formation of Er^{3+} cluster sites could enhance the probability of CR process, and then decreases the intensities of the green and red emissions under 980 nm excitation.

3.6. Stokes and anti-stokes luminescence spectra of Zn/Er:LiNbO$_3$ crystals

In order to determine the relationship between the defect structure and the optical characteristics of Er^{3+} ion in Er:LiNbO$_3$ crystal, Zn^{2+} and Er^{3+} ions codoping LiNbO$_3$ crystals are grown and discussed. Fig. 9 shows the stokes and anti-stokes luminescence spectra of Zn/Er:LiNbO$_3$ under different excitation wavelength. According to the previous works, 6 mol% Zn^{2+} ions codoping dissociates Er^{3+} cluster sites in LiNbO$_3$ crystal doped with 3 mol% Er^{3+} ions [27]. Based on the above proposed relation between the structure and the optical characteristics of Er^{3+} ion, the decreased Er^{3+} cluster sites in Zn/Er:LiNbO$_3$ crystal will result in the following conclusions. Firstly, under 476 nm excitation, the decreased Er^{3+} cluster sites corresponding to the increasing CR1, CR2 and CR3 processes (Fig. 5) will increase the population of $^4S_{3/2}$ state and the green emission. Secondly, by use of 800 nm excitation, the decreased Er^{3+} cluster sites will result in an enhancement of the green UC emission and in turn a weaker intensity of red UC emission. Finally, the decreased Er^{3+} cluster sites could lead to the reduction of the green and red UC emission under 980 nm excitation. These conclusions are consistent with the experimental results shown in Fig. 9.

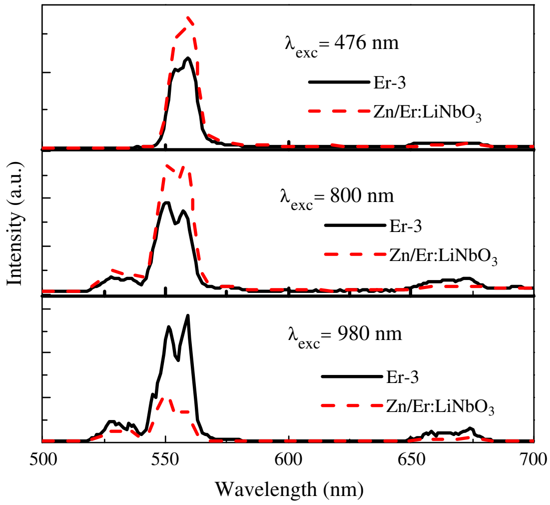

Fig. 9. The stokes and anti-stokes luminescence spectra of Er:LiNbO$_3$ crystal doped with and without 6 mol% Zn^{2+} ion under different excitation wavelength.

3.7. Near infrared emission spectra of Er:LiNbO$_3$ under 980 nm excitation

The near infrared emission spectra of Er:LiNbO$_3$ crystals under 980 nm excitation are shown in Fig. 10. The near infrared emission centered at 1540 nm is attributed to the $^4I_{13/2} \rightarrow {}^4I_{15/2}$ transition of Er^{3+} ion [28]. The intensity of 1.54 μm emission increases with the increasing concentration of Er^{3+} ions. The 1.54 μm emission has attracted much attention in the field of the remote sensing, coherent light detection and free-space communication [29,30]. The enhancement of 1.54 μm emission here meets the requirement of EDWA preparation, since the larger concentration of Er^{3+} ions could greatly shorten the optical diffusion route.

The Judd–Ofelt (J–O) theory is used to study the spectroscopic characteristics of Er^{3+} ion in Er:LiNbO$_3$ crystal [31–35]. The theoretical transition strength of Er^{3+} ion from an initial J to a final J' mainfold can be calculated by:

$$f_{the}(J \rightarrow J') = \frac{8\pi^2 mc}{3h(2J+1)\lambda}\left(X_{ed}\frac{S_{ed}}{e^2} + X_{md}\frac{S_{md}}{e^2}\right) \qquad (2)$$

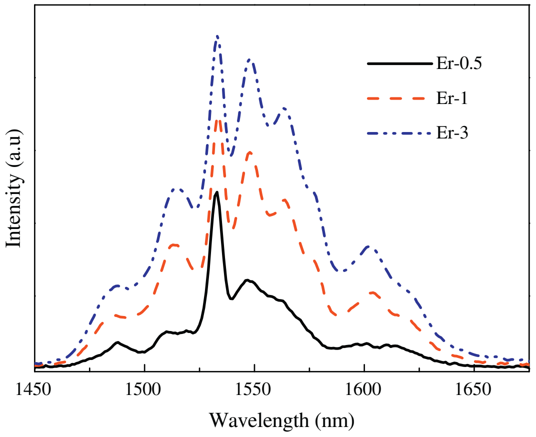

Fig. 10. Near infrared emission spectra of Er:LiNbO$_3$ crystals under 980 nm excitation.

where λ is barycentre wavelength at a given absorption band, m, c and h are the mass of the electron, light speed in vacuum and Planck's constant, respectively; S_{ed} and S_{md} are electric- and magnetic-dipole line strengths, respectively; X_{ed} and X_{md} are the local field electric and magnetic dipole correction factor, respectively, which can be calculated by equation [36]:

$$X_{ed(md)} = \frac{X_{ed(md)}(n_e) + X_{ed(md)}(n_o)}{2} \tag{3}$$

where n_o and n_e are ordinary and extraordinary refractive indices of $LiNbO_3$ crystal obtained from the Sellmeier equation [37].

The values of S_{ed} and S_{md} can be gained by the following equation:

$$S_{ed}(J \to J') = e^2 \sum_{t=2,4,6} \Omega_t |\langle SLJ||U^{(t)}||S'L'J'\rangle|^2 \tag{4}$$

$$S_{md}(J \to J') = \left(\frac{eh}{4\pi mc}\right)^2 |\langle SLJ||\overrightarrow{L} + 2\overrightarrow{S}||S'L'J'\rangle|^2 \tag{5}$$

The term $|\langle SLJ||U^{(t)}||S'L'J'\rangle|^2$, doubly reduced matrix elements of the unit-tensor operator $U^{(\lambda)}$, is independent on host material, and its value is tabulated in Ref. [38]. The transitions, except for the $^4I_{15/2} \to {}^4I_{13/2}$ transition, are assumed to be electric dipole in nature. The value of the magnetic-dipole transition strength (S_{md}) for the $^4I_{15/2} \to {}^4I_{13/2}$ transition is 70×10^{-8} [38].

According to the measured absorption spectra and the following equations, the experimental transition strength can be evaluated,

$$f_{\exp}(J \to J') = \frac{mc^2}{N\pi e^2 \lambda^2} \int \alpha(\lambda) d\lambda \tag{6}$$

$$\int \alpha(\lambda) d\lambda = \frac{1}{0.43d} \int OD(\lambda) d(\lambda) \tag{7}$$

where d is the thickness of the sample, $OD(\lambda)$ is the optical density, N is the number of rare earth ions per unit volume.

The accuracy of the fitting results can be validated by the root mean-square deviation (rms), which calculated equation is given by:

$$\delta_{rms} = \left(\frac{\sum_{J'=1}^{L} (f_{\exp} - f_{Jthe})^2}{L-3} \right)^{1/2} \tag{8}$$

where L is the number of the absorption bands involved in the fitting, f_{Jthe} is obtained by inducing the J–O parameters Ω_t (t = 2, 4 and 6) into Eq. (2).

The Einstein spontaneous emission probability A $(J \to J')$ is the sum of the probabilities for spontaneous emission of electric- (A_{ed}) and magnetic-dipole radiation (A_{md}) from an excited manifold J to a lower manifold J'. The values of A_{ed} $(J \to J')$ and A_{md} $(J \to J')$ are calculated from the two equations, respectively:

$$A_{ed}(J \to J') = \frac{64\pi^4 e^2}{3h(2J+1)\lambda^3} \frac{n(n^2+2)^2}{9} \sum_{t=2,4,6} \Omega_t |\langle SLJ||U^{(t)}||S'L'J'\rangle|^2 \tag{9}$$

$$A_{md}(J \to J') = \frac{4\pi^2 e^2 n^3 h}{3m^2 c^2 (2J+1)\lambda^3} |\langle SLJ||\overrightarrow{L} + 2\overrightarrow{S}||S'L'J'\rangle|^2 \tag{10}$$

The radiative lifetime τ_{rad} of the J manifold can be calculated by the formula:

$$\tau_J = 1/\sum_{J'} A(J \to J') \tag{11}$$

The fluorescence branching ratio for the $J \to J'$ transition:

$$\beta = A(J \to J')/\sum_{J'} A(J \to J') \tag{12}$$

where $\sum_{J'} A(J \to J')$ is the reciprocal of the total spontaneous emission probabilities.

Table 3 presents the experimental transition strengths ($f_{\exp}$), theoretical ones (f_{the}) and the corresponding root mean-square deviation (δ_{rms}) in Er-0.5, Er-1 and Er-3 crystals. The J–O intensity parameters Ω_t (t = 2, 4 and 6) are derived from the experimental oscillator strengths by a least-squares fitting approach and also illustrated in Table 3. As illustrated in Table 3, the parameters δ_{rms} are 4.31, 6.81 and 3.77×10^{-7}, respectively, for Er-0.5, Er-1 and Er-3 crystals. As for Er-1 crystal, the J–O intensity parameters are $\Omega_2 = 7.42 \times 10^{-20}$, $\Omega_4 = 3.40 \times 10^{-20}$ and $\Omega_6 = 1.75 \times 10^{-20}$ cm^2. J. Amin has been reported that the δ_{rms} is found to be 3.1×10^{-7} for $LiNbO_3$ crystal doped with 1 mol% Er^{3+} ions, and the J–O intensity parameters are $\Omega_2 = 7.29 \times 10^{-20}$, $\Omega_4 = 2.24 \times 10^{-20}$ and $\Omega_6 = 1.27 \times 10^{-20}$ cm^2 [25]. Since our calculated results are comparable to that reported by J. Amin, the fitting results of J–O theory here may be believable. The local asymmetry and the change in the environment of Er^{3+} ion in crystal lattice are mainly affected by Ω_2, and the intensity parameters Ω_4 and Ω_6 are mostly dependent on bulk properties. As shown in Table 3, the trend of $\Omega_2 > \Omega_4 > \Omega_6$ for Er^{3+} ions means that Er^{3+} ions are in a polarized environment. The decreased Ω_2 value, arising from the increasing concentration of Er^{3+} ion, indicates that the hypersensitive transitions $^4I_{15/2} \to {}^2H_{11/2}/{}^4G_{11/2}$ of Er^{3+} ions are affected by the Er^{3+} ion content. This is because Ω_2 is sensitive to the hypersensitive transitions. The spectroscopic quality factor X, defined by the ratio of the intensity parameter Ω_4 to Ω_6 ($X = \Omega_4/\Omega_6$), is an important predictor for stimulated emission in the laser active medium. The spectroscopic quality factor X is calculated to be 1.28, 1.94 and 3.93 for Er-0.5, Er-1 and Er-3 crystals, respectively. The largest spectroscopic quality factor X in Er-3 crystal suggests $LiNbO_3$ highly doped with Er^{3+} ions would be a promising candidate for laser medium.

The calculated radiative lifetimes (τ_{rad}) and fluorescence branching ratios (β) in Er:$LiNbO_3$ crystals are listed in Table 4. As shown in Table 4, the radiative lifetime of 1.54 μm emission in Er-1 crystal is 2123.3 μs, which is consistent with the accurate measurable experiment result (τ = 2300 μs) [39]. The radiative lifetime of 1.54 μm emission in Er-3 crystal lengthens up to 5722.7 μs. The long 1.54 μm lifetime in Er:$LiNbO_3$ is of key importance in the design of any practical device. The behavior that the fluorescence branching ratio β for the $^4S_{3/2}/{}^2H_{11/2} \to {}^4I_{15/2}$ transition decreases with the increasing Er^{3+} content favors the enhancement of 1.54 μm emission in Er-3 crystal.

Fig. 11 shows the absorption cross section (σ_{abs}) of 1.54 μm emission in Er-3 crystal, which is calculated by the following equation [40]:

$$\sigma_{abs}(\lambda) = 2.303 \frac{OD(\lambda)}{Nd} \tag{13}$$

where λ is the absorption wavelength, OD (λ) is the optical density, N is the concentration of Er^{3+} ion in the crystal, d is the thickness of the sample.

The emission cross section (σ_{em}) of 1.54 μm emission in Er-3 crystal, which is gained based on Füchtbauer–Ladenburg (FL) [41] and McCumber (MC) [42,43] theory (formulas (14) and (15), respectively), is also illustrated in Fig. 11.

$$\sigma_{eFL}(\lambda) = \frac{\lambda^4}{8\pi c n^2 \Delta\lambda_{eff}} A_{^4I_{13/2} \to {}^4I_{15/2}} \tag{14}$$

$$\sigma_{eMC}(\lambda) = \sigma_{abs}(\lambda) \frac{Z_l}{Z_u} \exp\left(\frac{E_{ZL} - hc/\lambda}{kT}\right) \tag{15}$$

Table 3
The theoretical and experimental transition strength, J–O intensity parameters Ω_t and the spectroscopic quality factor X of Er:LiNbO$_3$ crystals.

Transition $^4I_{15/2}\rightarrow$	Er-0.5		Er-1		Er-3	
	f_{exp}	f_{the}	f_{exp}	f_{the}	f_{exp}	f_{the}
$^4I_{13/2}$	157.6	154.6	165.44	168.1	105.5	106.0
$^4I_{11/2}$	71.26	49.23	56.84	46.79	34.70	17.17
$^4F_{9/2}$	152.9	138.5	225.8	209.6	135.5	114.4
$^4S_{3/2}$	31.23	32.77	29.79	38.00	20.54	12.10
$^2H_{11/2}$	1104	1022	828.1	710.4	457.9	386.4
$^4F_{7/2}$	141.0	138.2	172.3	178.8	107.6	75.33
$^4F_{3,5/2}$	52.38	66.03	70.00	76.38	46.92	24.30
$^2H_{9/2}$	61.96	53.94	72.49	65.62	46.59	23.90
$^4G_{11/2}$	1947	2019	1256	1400	716.2	760.9
$^4G_{9/2}$	102.2	108.4	130.3	171.4	132.7	100.8
Ω_2	12.5		7.42		3.89	
Ω_4	1.94		3.40		2.20	
Ω_6	1.51		1.75		0.56	
$X(\Omega_4/\Omega_6)$	1.28		1.94		3.93	
δ_{rms}	4.31		6.81		3.77	

Table 4
The radiative lifetime (τ_{rad}) and fluorescence branching ratios (β) in Er:LiNbO$_3$ crystals.

Transition	Er-0.5		Er-1		Er-3	
	β	τ_{rad}	β	τ_{rad}	β	τ_{rad}
$^4I_{13/2}\rightarrow{}^4I_{15/2}$	1	2458.5	1	2123.3	1	5722.7
$^4I_{11/2}\rightarrow{}^4I_{13/2}$	0.1258	1270.2	0.1433	1310.8	0.2021	3332.0
$^4I_{15/2}$	0.8742		0.8567		0.7979	
$^4I_{9/2}\rightarrow{}^4I_{11/2}$	0.0082	1369.3	0.0057	860.85	0.0078	1469.2
$^4I_{13/2}$	0.2306		0.1693		0.0947	
$^4I_{15/2}$	0.7611		0.8250		0.8975	
$^4F_{9/2}\rightarrow{}^4I_{9/2}$	0.0213	168.37	0.0134	114.53	0.0230	209.35
$^4I_{11/2}$	0.0434		0.0292		0.0193	
$^4I_{13/2}$	0.0462		0.0426		0.0449	
$^4I_{15/2}$	0.8892		0.9148		0.9128	
$^4S_{3/2}\rightarrow{}^4F_{9/2}$	≈0	146.91	≈0	126.09	≈0	390.05
$^4I_{9/2}$	0.0315		0.0359		0.0491	
$^4I_{11/2}$	0.0183		0.0188		0.0204	
$^4I_{13/2}$	0.2585		0.2572		0.2531	
$^4I_{15/2}$	0.6914		0.6878		0.6770	
$^2H_{11/2}\rightarrow{}^4F_{9/2}$	0.0028	15.678	0.0023	21.162	0.0021	33.89
$^4I_{9/2}$	0.0104		0.0103		0.0088	
$^4I_{11/2}$	0.1360		0.1839		0.2892	
$^4I_{13/2}$	0.0106		0.0138		0.0119	
$^4I_{15/2}$	0.8402		0.7896		0.6881	
$^2H_{9/2}\rightarrow{}^4F_{7/2}$	0.0021	30.062	0.0014	29.769	0.0011	42.81
$^2H_{11/2}$	0.0036		0.0040		0.0037	
$^4F_{9/2}$	0.141		0.1401		0.1987	
$^4I_{9/2}$	0.3203		0.3144		0.4480	
$^4I_{11/2}$	0.0778		0.0719		0.0629	
$^4I_{13/2}$	0.2746		0.2505		0.1714	
$^4I_{15/2}$	0.1806		0.2177		0.1141	

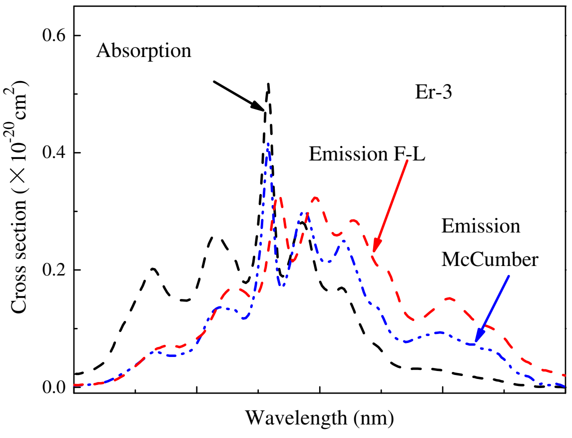

Fig. 11. The absorption and emission cross section spectra of Er-3 crystal.

In Eq. (14), λ is the wavelength of emission peak, and $\Delta\lambda_{eff}$ is the effective bandwidth of the 1.54 μm emission. The Einstein coefficient A (the transition strength from the $^4I_{13/2}$ to $^4I_{15/2}$ state) can be attained in Table 4. On the other hand, in Eq. (15), the ratio of Z_l/Z_u is equal to 0.8 [44], where Z_l and Z_u are the partition functions for the lower and upper levels involved in the considered optical transition, respectively. E_{ZL} is the energy of the zero-line between the lowest crystal field components of the electronic states. It can be seen from Fig. 11 that the calculated emission cross section (σ_{eMC}) based on MC theory are 0.416×10^{-20} cm^2 at 1529 nm. Based on FL theory, the emission cross sections (σ_{eFL}) at 1534 nm and 1548 nm are 0.330×10^{-20} and 0.324×10^{-20} cm^2, respectively. Although the peak shapes of the two emission cross sections are different, their maximum values are similar. Therefore, the calculated results are creditability. In comparison with the emission cross section of some other Er^{3+}-doped materials,

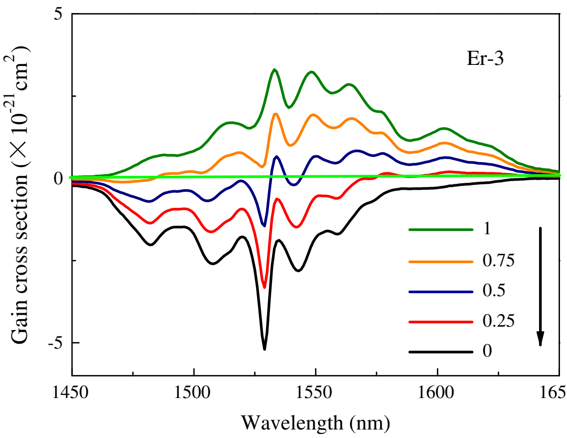

Fig. 12. Gain cross section spectra for the $^4I_{13/2} \rightarrow {}^4I_{15/2}$ transition as a function of P in Er-3 crystal.

such as Er:LaGaO$_3$ ($\sigma_{em} = 0.59 \times 10^{-20}$ cm^2) [45] and Er:YAG ($\sigma_{em} = 0.5 \times 10^{-20}$ cm^2) [46], Er-3 crystal could be considered as a promising laser-active material.

The gain cross section of $^4I_{13/2} \rightarrow {}^4I_{15/2}$ transition in Er-3 crystal as a function of P ranging from 0 to 1 is shown in Fig. 12. Gain cross sections are calculated based on the absorption and emission cross sections according to the following equation [47]:

$$g(\lambda) = P\sigma_{em}(\lambda) - (1 - P)\sigma_{abs}(\lambda) \tag{16}$$

where P is the excited state population fraction, defined as the ratio of the electron population densities of $^4I_{13/2}$ to that of $^4I_{15/2}$ state. As shown in Fig. 12, when P is equal to 0.5 the gain cross section spectrum is relatively flat in the 1549–1584 nm range, in agreement with the application in the C-band of telecommunications (1530–1560 nm) [48].

4. Conclusion

In this paper, the structural and optical characteristics of Er:LiNbO$_3$ crystals grown by Czochraski method have been investigated. Experimental results show that Er^{3+} cluster sites are formed in Er-3 crystal, which favor the increased probability of CR processes. The decreased green emission in Er-3 crystal is attributed to the increased CR processes ($^4S_{3/2} + {}^4I_{15/2} \rightarrow {}^4I_{9/2} + {}^4I_{13/2}$, $^4F_{7/2} + {}^4I_{15/2} \rightarrow {}^4I_{11/2} + {}^4I_{11/2}$ and $^2H_{11/2} + {}^4I_{11/2} \rightarrow {}^4F_{9/2} + {}^4F_{9/2}$) under 476 nm excitation. The drastically increased red UC emission of Er-3 arises from the enhanced CR processes probabilities ($^2H_{11/2} + {}^4I_{13/2} \rightarrow {}^4I_{11/2} + {}^4F_{9/2}$ and $^4F_{7/2} + {}^4I_{11/2} \rightarrow {}^4F_{9/2} + {}^4F_{9/2}$) under 800 nm excitation. As for Zn/Er:LiNbO$_3$ crystal, the decreased green and red UC emissions result from the dissociation of the Er^{3+} cluster sites which reduces the CR probabilities ($^4I_{11/2} + {}^4I_{11/2} \rightarrow {}^4F_{7/2} + {}^4I_{15/2}$ and $^4I_{13/2} + {}^4I_{11/2} \rightarrow {}^4F_{9/2} + {}^4I_{15/2}$). J–O intensity parameters Ω_2, Ω_4 and Ω_6 in Er-3 crystal are 3.89×10^{-20}, 2.20×10^{-20} and 0.56×10^{-20}, respectively, and the spectroscopic quality factor X is 3.93. The maximum emission cross sections based on MC and FL are 0.416×10^{-20} cm^2 at 1529 nm, and 0.330×10^{-20} and 0.324×10^{-20} cm^2 at 1534 nm and 1548 nm, respectively. The experimental results indicate that Er-3 crystal would be the potential laser operation around 1.54 μm emission.

Acknowledgements

We are grateful to National Natural Science Foundation of China (Nos. 10732100, 11232015, 11072271 and 10972239) and the Natural Science Foundation of Heilongjiang Province of China (B200903).

References

[1] J.B. Gruber, D.K. Sardar, R.M. Yow, B. Zandi, E.P. Kokanyan, Phys. Rev. B 69 (2004) 195103.
[2] L.H. Slooff, A. van Blaaderen, A. Polman, G.A. Hebbink, S.I. Klink, F.C.J.M. Van Veggel, D.N. Reinhoudt, J.W. Hofstraat, J. Appl. Phys. 91 (2002) 3955.
[3] J.J. Ju, T.Y. Kwon, S.I. Yun, M. Cha, H.J. Seo, Appl. Phys. Lett. 69 (1996) 1358.
[4] R. Lisiecki, G. Dominiak-Dzik, T. Łukasiewicz, W. Ryba-Romanowski, J. Mol. Struct. 704 (2004) 323.
[5] F. Auzel, Chem. Rev. 104 (2004) 139.
[6] J.W. Shur, W.S. Yang, S.J. Suh, J.H. Lee, T. Fukuda, D.H. Yoon, Cryst. Res. Technol. 37 (2002) 353.
[7] J.Y. Sun, J.B. Xian, H.Y. Du, J. Phys. Chem. Solids 72 (2011) 207.
[8] Hellmig, S. Salewski, A. Stark, J. Schwenke, P.E. Toschek, K. Sengstock, V.M. Baev, Opt. Lett. 35 (2010) 2263.
[9] N. Sdiri, H. Elhouichet, C. Barthou, M. Ferid, J. Mol. Struct. 1010 (2012) 85.
[10] Y.M. Yang, Z.P. Yang, P.L. Li, X. Li, Q.L. Guo, B.J. Chen, Opt. Mater. 32 (2009) 133.
[11] J.A. Lázaro, M.A. Rebolledo, J.A. Vallés, IEEE J. Quantum Electron. 37 (2001) 1460.
[12] H.Y. Fan, G.N. Wang, K.F. Li, L.L. Hu, Solid State Commun. 150 (2010) 1101.
[13] G.Y. Chen, H.C. Liu, G. Somesfalean, H.J. Liang, Z.G. Zhang, Nanotechnology 20 (2009) 385704.
[14] F. Vetrone, J.C. Boyer, J.A. Capobianco, A. Speghini, M. Bettinelli, Chem. Mater. 15 (2003) 2737.
[15] L. Sun, A.H. Li, F.Y. Guo, Q. Lü, Y.H. Xu, L.C. Zhao, Appl. Phys. Lett. 91 (2007) 071914.
[16] P. Lerner, C. Legras, J.P. Dumas, J. Cryst. Growth 3–4 (1968) 231.
[17] X.H. Zhen, Q. Li, H.T. Li, Z.L. Liu, Y.H. Xu, L.C. Zhao, J. Lumin. 114 (2005) 288.
[18] L. Sun, C.H. Yang, A.H. Li, Y.H. Xu, L.C. Zhao, J. Appl. Phys. 105 (2009) 043512.
[19] Z.H. Hu, P. Guo, J.Y. Li, X.H. Zhen, Cryst. Res. Technol. 42 (2007) 488.
[20] W.Q. Shi, M. Bass, M. Birnbaum, J. Opt. Soc. Am. B 7 (1990) 1456.
[21] D.M. Gill, L. McCaughan, J.C. Wright, Phys. Rev. B 53 (1996) 2334.
[22] F. Liu, E. Ma, D.Q. Chen, Y.L. Yu, Y.S. Wang, J. Phys. Chem. B 110 (2006) 20843.
[23] F. Pandozzi, F. Vetrone, J.C. Boyer, R. Naccache, J.A. Capobianco, A. Speghini, M. Bettinelli, J. Phys. Chem. B. 109 (2005) 17400.
[24] Y.N. Qian, R. Wang, L.L. Xing, Y.L. Xu, C.H. Yang, Chem. Res. Chinese Univ. 28 (2012) 295.
[25] J. Amin, B. Dussardier, T. Schweizer, M. Hempstead, J. Lumin. 69 (1996) 17.
[26] X. Wang, G.Y. Shan, K.F. Chao, Y.L. Zhang, R.L. Liu, L.Y. Feng, Q.H. Zeng, Y.J. Sun, Y.C. Liu, X.G. Kong, Mater. Chem. Phys. 99 (2006) 370.
[27] Y.N. Qian, R. Wang, C. Xu, L.L. Xing, Y.L. Xu, C.H. Yang, J. Rare Earths 30 (2012) 25.
[28] S.Z. Lu, Q.H. Yang, B. Zhang, H.J. Zhang, Opt. Mater. 33 (2011) 746.
[29] J.H. Yang, S.X. Dai, N.L. Dai, L. Wen, L.L. Hu, Z.G. Jiang, J. Lumin. 106 (2004) 9.
[30] C. Lira, E. Martín-Rodríguez, R. Martínez-Martínez, I. Camarillo, G.H. Muñoz, J. Garcia-Solé, U. Caldiño, Opt. Mater. 32 (2010) 1266.
[31] M. Reddy, B.S. Reddy, G.R. Dillip, K. Mallikarjuna, B.D.P. Raju, J. Mol. Struct. 1019 (2012) 166.
[32] O. Ravi, C.M. Reddy, L. Manoj, B.D.P. Raju, J. Mol. Struct. 1029 (2012) 53.
[33] M.D. Shinn, W.A. Sibley, M.G. Drexhage, R.N. Brown, Phys. Rev. B 27 (1983) 6635.
[34] M.P. Hehlen, N.J. Cockroft, T.R. Gosnell, A.J. Bruce, Phys. Rev. B 56 (1997) 9302.
[35] H. Ping, D.Q. Chen, Y.L. Yu, Y.S. Wang, J. Alloys Compd. 490 (2010) 74.
[36] T.S. Lomheim, L.G. DeShazer, J. Appl. Phys. 49 (1978) 5517.
[37] U. Schlarb, K. Betzler, Phys. Rev. B 48 (1993) 15613.
[38] M.J. Weber, Phys. Rev. 157 (1967) 262.
[39] D.L. Zhang, E.Y.B. Pun, J. Appl. Phys. 94 (2003) 1339.
[40] J.H. Xie, Q. Zhang, Y.X. Zhuang, X.F. Liu, M.J. Guan, B. Zhu, R. Yang, J.R. Qiu, J. Alloy Compd. 509 (2011) 3032.
[41] U. Hömmerich, C. Hanley, E. Brown, S.B. Trivedi, J.M. Zavada, J. Alloys Compd. 488 (2009) 624.
[42] D.E. McCumber, Phys. Rev. 134 (1964) 299.
[43] N. Jaba, H.B. Mansour, A. Kanoun, A. Brenier, B. Champagnon, J. Lumin. 129 (2009) 270.
[44] C.H. Huang, L. McCaughan, D.M. Gill, J. Lightwave Technol. 12 (1994) 803.
[45] Sokólska, Appl. Phys. B 71 (2000) 157.
[46] H. Stange, K. Petermann, G. Huber, E.W. Duczynski, Appl. Phys. B 49 (1989) 269.
[47] H. Xie, Q. Zhang, Y.X. Zhuang, X.F. Liu, M.J. Guan, B. Zhu, R. Yang, J.R. Qiu, J. Alloy Compd. 509 (2011) 3032.
[48] S.W. Harun, R. Parvizi, X.S. Cheng, A. Parvizi, S.D. Emami, H. Arof, H. Ahmad, Opt. Laser Technol. 42 (2010) 790.